Structural insights into GTP-coupled conformational changes in Mfn1 revealed by time-resolved transition metal ion FRET.

Hurwitz, S.M.[a], Zagotta, W.N.[b], Gordon, S.E. [b], *Hoppins, S[a].

Author Affiliations:
a Department of Biochemistry, University of Washington, Seattle, WA 98195
b Department of Neurobiology and Biophysics, University of Washington, Seattle, WA 98195

*Corresponding author:
Suzanne Hoppins
University of Washington
Department of Biochemistry
1959 NE Pacific Street
Health Sciences Building, J383
Seattle, WA 98195
Phone (206) 616 7565
Fax (206) 685 1792
e-mail: shoppins@uw.edu
ORCID – orcid/org/0000-0002-8070-3560

Abstract

Outer mitochondrial membrane fusion is mediated by the mitofusin paralogs Mfn1 and Mfn2. Nucleotide-driven self-assembly and conformational changes are required for regulated membrane fusion activity, but the allosteric mechanisms remain enigmatic due to incomplete structural information. In this study, we investigate the GTP-coupled conformational dynamics of Mfn1 using time-resolved transition metal ion fluorescence resonance energy transfer (tmFRET). Using the minimal Mfn1 construct with the GTPase domain and helical bundle 1 (HB1) connected by Hinge 2, we engineered FRET pairs by incorporating a fluorescent noncanonical amino acid donor and a metal ion acceptor. For each state of the catalytic cycle, we measured tmFRET with fluorescence lifetimes and determined distance distributions, which can capture complex structural heterogeneity. Our distance measurements for the GDP-bound state matched predictions from the atomic resolution structure, establishing that the same open state, with GTPase and HB2 domains far apart, exists in solution. Our findings reveal that the previously reported transition state is not a single closed state in solution. Rather, the distance distributions indicate that the presence of GDP+Pi results in an equilibrium between the open and closed state. For the first time, we capture the GTP-bound and nucleotide free states of Mfn1. GTP binding favors the open state, revealing an unrecognized conformational change in the fusion mechanism driven by GTP hydrolysis. Finally, the conformation of the apo state is distinct from each nucleotide bound state. Our data reveal fundamental insights into the structures and energetics of GTP-driven conformational changes of Mfn1.

Significance (120 words)

The dynamin superfamily of proteins (DSPs) mediate diverse membrane remodeling events. DSP self-assembly and conformational changes are regulated by GTP binding and hydrolysis, but the allosteric mechanisms are not well understood. The mitofusins are DSPs that mediate mitochondrial outer membrane fusion, a process essential for the regulation and maintenance of mitochondrial function. Using time-resolved transition metal ion fluorescence resonance energy transfer (tm-FRET) we obtain structural information for the entire catalytic cycle of Mfn1. This includes the GTP-bound and nucleotide free states, which were not accessible with other methods. In addition, we provide insight into the energetics of GTP hydrolysis and the accessibility of the closed state, where the GTPase and HB1 domains interact.

Introduction

Eukaryotic cells are functionally compartmentalized by membrane bound organelles. These organelle membranes are dynamic, and ongoing fusion and fission events play essential roles in protein and lipid trafficking as well as in quality control mechanisms. The fusion and fission of diverse cellular membranes are mediated by the dynamin superfamily of proteins (DSPs)(1, 2). DSPs are mechanochemical enzymes that hydrolyze GTP. DSPs have shared domain organization, including a globular GTPase domain, helical bundle domains, and a lipid-interacting/targeting domain. Universally, GTP allosterically regulates conformational changes in DSPs to drive assembly and membrane remodeling (1, 3, 4).

Mechanistic understanding of the DSP family is largely derived from studies of dynamin and dynamin-related protein 1 (Drp1). Both utilize mechano-constriction to catalyze fission of their target membranes (plasma membrane and mitochondria, respectively) (5, 6). Our mechanistic understanding of fission DSPs has benefited from the accumulation of structural information that captures different conformational states, although allosteric regulation at the individual protein level remains largely undefined (1, 3, 7–9).

Less is known about the mechanism of fusion DSPs, including the mitofusin paralogs, Mfn1 and Mfn2. The mitofusins are localized to the mitochondrial outer membrane and together mediate fusion of this membrane (10–12). In concert, mitochondrial fusion, fission and microtubule-based transport regulate mitochondrial size, shape, and distribution throughout the cell (13–18). These dynamic properties are also essential to maintain and modulate mitochondrial functions such as metabolism, calcium levels, and apoptosis. Dysregulation of mitochondrial fusion resulting from mutations in *MFN2* causes the neurodegenerative disease Charcot Marie Tooth Type 2A (CMT2A) (19–21). Other neurogenerative diseases including ALS, Alzheimer's, and Parkinsons disease are also associated with aberrant mitochondrial dynamics and mitochondrial dysfunction, highlighting the broad importance of mitochondrial dynamics (22–25).

Mitofusin-mediated membrane fusion occurs in discrete steps that are dictated by the catalytic cycle (Fig. 1A)(26). The mitofusin GTPase domain forms an extensive intermolecular interface when bound to GTP (27–30). One model for membrane tethering, the first step of fusion, is that this interface forms across two membranes, or in *trans* (26). A second model posits that the mitofusin tethering complex is formed via intermolecular interactions of the C-terminal domain (18, 31). Importantly, the conformation of the mitofusins when GTP is bound, and therefore the initial tethering step, remains unknown. Progression from tethering to lipid mixing requires that the mitofusin tethering complex dynamically rearranges to pull the opposing membranes together and promote lipid mixing. This likely requires a large conformational change, which is hypothesized to be driven allosteric changes coupled to the progressive steps of GTP hydrolysis. Following lipid mixing, disassembly of the fusion complex would include the dissolution of the G-G interface when the catalytic cycle is complete and mitofusin is in the apo state. While this is likely a key feature of disassembly, the conformation of the apo state is not known.

Structural studies have provided some key insights into the mechanism of mitofusin-mediated fusion (27–30). Whereas the structure of full-length mitofusin remains elusive, a minimal GTPase domain construct, mini-Mfn1, containing the GTPase domain and helical bundle 1 (HB1) has provided atomic resolution structures for two nucleotide-bound states (27–29). Specifically, the transition state, representing mini-Mfn1 bound to GDP+Pi, is stabilized by salt-bridge contacts between the GTPase domain and HB1 and is referred to as the closed state (Fig. 1A) (29). Following the release of Pi, the interaction between the GTPase domain and HB1 is no longer favorable and HB1 moves away from the GTPase domain resulting in a conformation referred to as the open state. The role of this large domain rearrangement in the fusion mechanism is unknown. The absence of structural information for the GTP-bound state leaves an open question as to whether this is the only large conformation change required for mitofusin-mediated membrane fusion.

To define the conformational dynamics of mitofusin throughout the catalytic cycle, we leveraged our novel transition metal ion fluorescence resonance energy transfer (tmFRET) approach (32). tmFRET utilizes a donor fluorophore and transition metal ion acceptor site-specifically incorporated in a protein. The donor is a fluorescent non-canonical amino acid and the acceptor is a non-fluorescent Cu(II) bound to a metal chelator covalently attached to a solvent accessible cysteine (33). tmFRET can measure distances in the range of 10-50 Å, ideal for analyzing protein conformational changes (34, 35). As in classical FRET, the distance between the donor-acceptor pair dictates the FRET efficiency and can be used as a molecular ruler to measure distances between sites on a protein and therefore report different conformational states (Fig. 1B)(36).

To apply the tmFRET system to Mfn1, we utilized mini-Mfn1 (27–29). While mini-Mfn1 has a large internal truncation removing HB2 and the TMD, the presence of the C-terminal helix in HB1 is consistent with the domain architecture of the DSP family (4, 37). There is also some controversy regarding the topology of Mfn1 (38), but protease protection and C-terminal tagging experiments from our lab support the model that both termini are in the cytosol (39, 40). The mini-Mfn1 construct is an ideal tool since it has robust expression, well developed purification protocols, and a straightforward functional readout (GTPase activity). Furthermore, the available structures of mini-Mfn1 provide a resource to design donor-acceptor pairs with predicted distances within FRET range.

In this study we used time resolved tmFRET, quantifying the fluorescent lifetimes of the donor to report FRET efficiency. The fluorescence lifetime, or time between excitation and emission of a photon, is typically on the order of a few nanoseconds (36). Time-resolved FRET has the advantage of recording FRET efficiencies from an entire population of protein in solution in nanosecond snapshot (41–43). This captures distance distributions of the donor-acceptor pair and reveals structural heterogeneity in the protein sample. This heterogeneity can arise from rotameric variations of both the donor and acceptor, flexibility of the sample in the conformational state, and multiple conformational states in the sample. In the time-domain, a

histogram of the lifetimes of a fluorophore with a single exponential lifetime appears as a single exponential decay (linear on a semi-log graph) (Fig. 1C, black). FRET resulting from a single donor-acceptor distance will shorten the lifetime while maintaining the single exponential decay (Fig. 1C, magenta). However, when there are multiple distances, such as from a population of protein in different conformations, the lifetime decay will be multi-exponential with contributions from all donor-acceptor distances in the sample (Fig. 1C, blue-dashed).

This approach allowed us to capture structural information for each step of the mitofusin catalytic cycle. Our tmFRET data for mini-Mfn1 in the presence of GDP are in good agreement with the open state crystal structure, establishing that this conformation exists in solution. Interestingly, we found that in the transition state (GDP+Pi) mini-Mfn1 was structurally heterogeneous, with about 60% of the protein in the closed conformation and the rest in the open conformation. Thus, like other ligand-dependent conformational changes we have reported, the energetic landscape of the transition state is such that mini-Mfn1 favors the closed state (41, 42). Our approach allowed analysis of both the GTP-bound and apo-mini-Mfn1 for the first time. We show that the GTP-bound mini-Mfn1 was comparable to the open, GDP-bound state. This establishes that both GTP hydrolysis and the release of the free phosphate cause large conformational changes. Finally, a novel conformational state was identified when no nucleotide is bound to mini-Mfn1, probably of relevance to disassembly. In sum, the data presented here represent the first complete analysis of the conformational dynamics of any DSP in solution throughout the catalytic cycle.

Results

Generation of the mini-Mfn1 donor-acceptor pair.

We sought to use the non-canonical amino acid Acridonylalanine (Acd) as the fluorescence donor and $[Cu(cyclenM)]^{2+}$ as the tmFRET acceptor (Fig. 1B). This donor-acceptor pair has a short R_0 (the distance which produces 50% FRET efficiency) of 15.3Å, allowing us to monitor only intramolecular FRET, even when mini-Mfn1 is dimerized in the presence of nucleotide. The metal ion acceptor requires a single solvent accessible cysteine to react with the metal ion chelator. We designed our donor and acceptor sites in HB1 and the GTPase domain, respectively, on either side of the hinge connecting these domains (see Fig. 3A).

There are six native cysteine residues in the GTPase domain, which were all solvent accessible in solution (data not shown). Therefore, we first engineered a cysteine-less construct by systematically replacing each cysteine with either alanine or serine, depending on which substitution supported higher expression and robust purification. The GTPase activity of the mini-Mfn1-noC construct was comparable to wild-type protein, indicating that these substitutions did not appreciably alter the catalytic properties (Fig. 2A). To confirm that this construct was functional in the context of full-length Mfn1 in cells, we scored mitochondrial morphology in Mfn1-null mouse embryonic fibroblasts expressing mNeonGreen-Mfn1 variants (Fig. 2B-C). Cells with empty vector possessed a fragmented mitochondrial network, consistent

with reduced mitochondrial fusion in the absence of Mfn1. Expression of either murine or human mNeonGreen-Mfn1 restored the reticular mitochondrial network, rescuing the null phenotype. Importantly, we also observed reticular mitochondrial networks in cells expressing a construct of human Mfn1 with the same serine/alanine substitutions in the GTPase domain as generated in mini-Mfn1-noC. This is consistent with this variant supporting mitochondrial fusion activity that is comparable to wild type.

We engineered the donor site in the first helix of HB1. At this site (L13), we incorporated Acd by amber codon suppression as previously described (33). Coomassie blue staining and in-gel fluorescence of purified TwinStrep-mini-Mfn1 indicate that Acd was successfully incorporated (Fig. 2D). Integration of Acd at only L13 was also supported by mass spectrometry analysis, which revealed no off-target Acd incorporation (Fig. S1). The L13Acd construct lacking the acceptor cysteine (donor only) was used as a negative control in all tmFRET experiments. We then introduced the metal-ion acceptor site at R171, which is predicted to be within tmFRET range from L13 in both the open and closed states (13.8 and 24.0Å, respectively). This construct (mini-Mfn1-L13Acd-R171C) also expressed robustly (Fig. 2E). The GTPase activity of mini-Mfn1-L13Acd-R171C was also comparable to wild-type controls (Fig. 2F), indicating that these mutations did not alter catalytic activity.

Time-resolved tm-FRET reveals distance distributions of mini-Mfn1 in GDP- and transition-bound states.

With our functional mini-Mfn1-L13Acd-R171C protein, we next sought to measure the donor-acceptor distances, starting with the two ligands previously used for X-ray crystallography, GDP and GDP•BeF_3 (Fig. 3A, D). We measured fluorescence lifetimes in the form of time-correlated single photon counting (TCSPC) decays. We first established the lifetime of the donor-only mini-Mfn1-L13Acd-noC in the presence of saturating GDP (brown trace, Fig. 3B), which produced decays similar to that of Acd-incorporated proteins reported previously (42). We then measured the lifetime of Acd in the donor only mini-Mfn1-L13Acd-noC protein construct in the presence of $[Cu(cyclenM)]^{2+}$, which is not expected to react with this cysteineless protein (gray trace, Fig. 3B). As expected, this lifetime was very similar to that obtained in the absence of $[Cu(cyclenM)]^{2+}$. Similar results were obtained for the donor-only mini-Mfn1-L13Acd-noC in the presence of saturating GDP•BeF_3 (Fig. 3E). This demonstrates that $[Cu(cyclenM)]^{2+}$ in the buffer did not result in FRET with the Acd in the protein and did not modify the donor only protein at non-specific sites near the Acd.

We next measured the lifetime of the complete tmFRET construct, mini-Mfn1-L13Acd-R171C-$[Cu(cyclenM)]^{2+}$, in the presence of GDP. The acceptor decreased the overall lifetime of Acd, consistent with FRET (magenta, Fig. 3B). We fit the lifetimes with a model that assumes a Gaussian distribution of donor-acceptor distances. The average distance ($\bar{r}$) and standard deviations (σ) from multiple experiments are shown in a spaghetti plot in Figure 3C with a mean distance $\bar{r}$ = 15.1 Å and standard deviation σ = 3.5 Å. To generate a predicted distance

distribution for comparison to our experimental data, we used chiLife. ChiLife is a software that predicts all the donor and acceptor rotamers on the stationary structure of Mfn1 bound to GDP (PDB:5YEW) to yield a distance distribution of the pair (Fig. 3A) (44). The distance distribution predicted by chiLife is overlayed on the spaghetti plot and has an average $\bar{r}$ = 13.8 Å and σ = 2.7 Å (dotted line). In this case, there is strong agreement between the prediction and our experimentally determined distribution for both the average distance and the standard deviation (Fig. 3C).

The same experiments were performed with mini-Mfn1-L13Acd-R171C-$[Cu(cyclenM)]^{2+}$ in the presence of saturating GDP•BeF_3 (blue, Fig. 3E). Compared to GDP conditions, we measured a smaller change in lifetime before and after labeling with $[Cu(cyclenM)]^{2+}$ in the GDP•BeF_3 condition. This is consistent with the prediction that the donor-acceptor pair is greater in the closed, GDP•BeF_3-bound state compared to the GDP-bound state (Fig. 3A, D). The distance distributions fit to a single state for GDP•BeF_3-mini-Mfn1 are summarized as spaghetti plots in Figure 3F, with an average $\bar{r}$ = 20.1 Å and σ = 6.3 Å. The chiLife prediction is overlayed on the spaghetti plot and has an average $\bar{r}$ = 24.0 Å and σ = 2.8 Å (black-dashed). Compared to the chiLife prediction, the experimental average distance between the donor-acceptor pair is smaller and the sigma is larger, resulting in a shifted and wider Gaussian curve. These data are consistent with the HB1 and the GTPase domains being further apart than observed in the crystal structure with greater conformational heterogeneity than predicted based on rotomeric movement.

Given the large sigma, we also considered the possibility that the data represents the presence of two populations - one in the closed state and the second in the open state. This would be consistent with a model where GDP•BeF_3 alters the energetics of mini-Mfn1, making the closed state accessible. To test whether our data support a distribution of the protein among two conformational states, we fit the data with a model that specified two Gaussians, our experimental GDP-mini-Mfn1 and the chiLife prediction of the closed state. The fraction in the closed state (f_{A2}), and therefore the distribution among the two Gaussians, was allowed to vary. In the context of this two-state model, our data indicate that about 60% of mini-Mfn1 is in the closed conformation in the presence of GDP•BeF_3 (Fig. 3G). We obtained similar chisquared values from fits with both single- and two-state models to our data indicating that they are statistically equivalent.

A known functional variant supports the two-state model of GDP•BeF_3 bound mini-Mfn1.

We set out to distinguish between the accuracy of the one and two-state models utilizing a known functional variant: R73Q. The GDP•BeF_3 crystal structure identified salt bridges between R73 in HB1 and D200 and D198 in the GTPase domain (29). The importance of the salt-bridges was demonstrated by characterizing variants with charge reversal substitutions. These variants possessed defects in dimerization *in vitro* and in mediating mitochondrial fusion in cells. In addition, a common CMT2A-related R→Q variant was assessed by bulk FRET experiments with purified mini-Mfn1-R73Q to show that this variant cannot form the closed conformation (29).

These data all support a model where these salt bridges stabilize the closed state when GDP•BeF_3 is bound.

Therefore, we created the R73Q substitution in our mini-Mfn1-L13Acd-R171C construct to further assess the two-state model. If GDP•BeF_3-mini-Mfn1 exists in a single state with 20 Å distance between the donor and acceptor, we expect that the substitution of R73Q will induce a third novel conformational state with an $\bar{r}$ between the GDP and GDP•BeF_3-bound values; however, if GDP•BeF_3-mini-Mfn1 is in equilibrium between the open and closed states, we expect that the R73Q variant will be only in the open state.

We first measured the lifetime decays of mini-Mfn1-L13Acd-R73Q-R171C before and after adding $[Cu(cyclenM)]^{2+}$ in the presence of GDP (Fig. 4A). A summary of these experiments is shown in the spaghetti plot in Figure 4B with the average experimental GDP-mini-Mfn1 distribution plotted in the dashed line. This revealed an average distance distribution of $\bar{r}$ = 15.2 Å (σ = 4.6 Å) for the mini-Mfn1-L13Acd-R73Q-R171C, similar the wild-type protein. This suggests the salt bridge has little or no effect on the structure or energetics of the GDP bound state, as expected from the crystal structure.

We then measured the lifetime decay of mini-Mfn1-L13Acd-R73Q-R171C before and after adding $[Cu(cyclenM)]^{2+}$ in the presence of GDP•BeF_3 (Fig. 4C). A summary of these experiments is shown in the spaghetti plot in Figure 4D with an average distance distribution of $\bar{r}$ = 14.8 (σ = 3.8 Å). This distance is comparable only to the GDP-bound state (Fig. 4E). These data suggest that the energetics of the Mfn1-R73Q variant in the presence GDP•BeF_3 strongly favor the open state, with little-to-no probability of being in the closed state. The fact that the distance distribution of mini-Mfn1-R73Q matches the open GDP-bound state with a small standard deviation supports the two-state model for the GDP•BeF_3 condition.

The proportion of molecules in each state can be converted into a change in the Gibbs free energy (ΔG) for the transition of HB1 relative to the GTPase domain from open to closed. For wild-type mini-Mfn1, the lifetime model of GDP•BeF_3 yielded ΔG= -0.21 kcal/mol, making the conformational change from open to closed energetically favorable. This represents the only known nucleotide condition where the closed state is favored. Given that mini-Mfn1-R73Q cannot access the closed conformation, the inter-domain salt bridges contribute significantly to this energetic effect.

Non-hydrolyzable GTP analogs induce the open conformation of mini-Mfn1.

We next sought to acquire structural information for mini-Mfn1 in the GTP-bound state, which was not obtained in previous characterizations (27–29). To do this, we utilized two different non-hydrolyzable GTP analogs since it has been previously shown that each non-hydrolyzable GTP analog can result in slight functional differences in DSPs (45, 46). We measured the lifetime decays of mini-Mfn1-L13Acd-R171C with either GTPγS or GMP-PNP before and after adding

$[Cu(cyclenM)]^{2+}$ (Fig. 5A & B). This revealed average distances of $\bar{r}$ = 14.6 Å (σ = 3.7 Å) when incubated with GTPyS and $\bar{r}$ = 15.5 Å (σ = 3.6 Å) with GMP-PNP (Fig. 5C & D). As illustrated by the overlay of the average distribution of the non-hydrolyzable GTP analogs and our experimental GDP distribution data, there is minimal difference in the donor-acceptor distance distributions (Fig. 5E). Based on these data we conclude that the GTP bound state is comparable to the open, GDP-bound conformation. This demonstrates that the closed conformation is only favored following GTP hydrolysis, when GDP+Pi is in the nucleotide pocket. Consequently, our data reveal an unappreciated conformational change during the catalytic cycle, supporting a model where the same large conformational change occurs and is reversed during mitofusin-mediated fusion: a domain closure when the GTP is hydrolyzed to GDP+Pi, and a reopening when the inorganic phosphate is released.

Time resolved tmFRET reveals a novel conformation when mini-Mfn1 is not bound to nucleotide.

Our data have provided structural insight into every nucleotide bound state in the catalytic cycle of Mfn1 but there is currently no structural information for the apo state. Therefore, we next assessed the conformation of mini-Mfn1 in the absence of nucleotide, which occurs before and after GTP hydrolysis. Importantly, this is the only state in which mini-Mfn1 will be a monomer as GTP-binding is required to form the G-G interphase that mediates dimerization of this construct. We measured the lifetime of mini-Mfn1-L13Acd-R171C with no nucleotide before and after adding $[Cu(cyclenM)]^{2+}$ (Fig. 6A). A summary of these experiments is shown in the spaghetti plot in Figure 6B. Under these conditions, we calculated an average distance between the donor and acceptor of $\bar{r}$ = 16.3 Å and σ = 4.4 Å. While both GTP-bound and GDP-bound exhibit average distances of ~15Å between the FRET pair, the apo state consistently results in a distance slightly greater than 16Å, suggesting this a unique conformational state. Furthermore, the σ is larger for apo-mini-Mfn1 compared to the GDP-bound state, indicating increased flexibility of this conformational state (Fig. 6C-E).

To further validate the intermediate apo state, we utilized another functional variant: Mfn1-R238A. This arginine residue has been shown to form a salt-bridge across the G-G interface. The Mfn1-R238A variant is catalytic dead, unable to dimerize via the G-G interface and therefore does not hydrolyze GTP (27). In the presence of each ligand, Mfn1-R238A recapitulated the apo state, supporting it as a one-state system with a unique conformation (Fig. S2). Given that the apo state would occur at the end of the catalytic cycle and promote dissolution of the G-G interface, it is likely a key step in the disassembly of Mfn1 post fusion.

Discussion

Here, we established a time-resolved tmFRET system to measure the conformational dynamics of mini-Mfn1 throughout the entire GTP catalytic cycle. This allowed us to acquire structural

information for every step of the catalytic cycle, which was not possible with previous approaches. Time-resolved tmFRET reliably provides valuable structural information in the form of average distances of each conformational state, heterogeneity of the distance for each conformation, and the relative proportion of different conformations (energetics) in a population.

We have obtained several novel insights into the GTP-dependent allosteric regulation of Mfn1 (summarized in Fig. 7). First, our data revealed the conformational state of Mfn1 in the GTP-bound state. GTP-binding is associated with the formation of the tethering complex, and our data indicate that Hinge 2 is in the open state in this complex. Second, we obtained novel insight into the catalytic step following GTP hydrolysis, where Mfn1 was proposed to undergo a large conformational change such that HB1 interacts with the GTPase domain. Our data show that the transition state results in an equilibrium between the closed and open states. The energetic calculations demonstrate that about 60% of the population is in the closed state. This conclusion was supported by our analysis of mini-Mfn1-R73Q, which alters the salt-bridge network between the GTPase and HB1 domains, and was only in the open state. Previous bulk FRET approaches to study the open-to-closed conformational change utilized fluorescence intensity to calculate FRET (29). In this case, the change in FRET intensity could only identify the average conformational change of the population, but not the proportion of mini-Mfn1 in each state. Third, our analysis of the GDP-bound state revealed a calculated distance in solution that is remarkably comparable to chiLife predictions. Together with our novel GTP-bound conformational data, we can now propose a model of mitofusin-mediated fusion where the open GDP-bound state represents a second conformational change back to a relatively stable open state. Finally, this approach also enabled the first structural analysis of Mfn1 in the absence of nucleotide and uncovered a novel conformational state with more conformational heterogeneity than observed in the GTP- and GDP-bound states. This conformation is likely significant for the disassembly of the fusion complex and therefore a key step in the mechanism.

One key limitation to our work is the use of the truncated mini-Mfn1, which is missing HB2 and is not embedded into the outer mitochondrial membrane. Both are essential aspects of the mechanism of mitofusin-mediated fusion and could alter the dynamics of Hinge 2 throughout hydrolysis. Furthermore, as the allosterically regulated conformational changes are predicted to propagate throughout the entire protein, we currently lack essential information about the allosteric regulation of HB2 and the role of the membrane throughout the catalytic cycle. Nonetheless, this system has revealed fundamental aspects of the conformational dynamics of Mfn1, exemplified by the fact that we identified two conformational states that had not previously been explored.

Future work will expand to applying this system to the other mitofusin paralog, Mfn2. Importantly, Mfn1 and Mfn2 that have fundamental differences in catalytic function, with mini-Mfn2 having an 8-fold lower hydrolysis rate compared to mini-Mfn1 (30). Furthermore, past work has shown that mitochondrial fusion is most efficient when the different paralogs are on opposing membranes (10). The heterotypic tethering complex could result in altered

conformational energetics of each paralog to increase fusion efficiency. Alternatively, distinct conformational dynamics of each paralog on each membrane may be essential for efficient membrane fusion. We now have the tools in-hand to test these models. Additionally, this system can expand to work that defines changes in conformational dynamics associated with mitochondrial fusion defects and/or disease. For example, CMT2A variants with dysfunctional lipid mixing have been previously characterized, including Mfn1-F202L and Mfn1-S329P (39, 47). In the context of mini-Mfn1, these variants do not have altered GTPase activity, and both can dimerize via the GTPase domain. Full-length Mfn1-F202L is capable of fusion, albeit at a decreased efficiency to the native Mfn1. In contrast, while Mfn1-S329P initiates fusion, it is incapable of facilitating lipid mixing. Identifying the conformational dynamics of these variants will provide key information to connect conformational dynamics with steps in the membrane fusion process. This would combine the protein structure, catalytic cycle, and the fusion mechanism into one concrete model. Finally, applying the system to full-length Mfn1 and Mfn2 would provide a more complete picture of allosteric regulation in the context of every domain and the membrane.

Methods

Constructs and Mutagenesis. The mini-Mfn1 construct was made by inserting the Mfn1-IM sequence from the $Mfn1_{IM}C$ pET28 plasmid (29, 39) into the pETM11 vector (Uniprot accession #E0R11) followed by a GSSG, two TEV protease cleavage sites and a Twin-Strep-tag sequence using Gibson assembly. All mutations were made by Gibson assembly. Specifically, $Mfn1_{NoC}$ changed six native cystines to create Mfn1-C111S-C156A-C167A-C196A-C260S-C327A-IM. The amber stop codon (TAG) replaced L13 to facilitate integration of Acd. To generate a construct with both a donor and acceptor site, a single cysteine mutation was introduced into the donor-only construct with no native cystines at sites $Mfn1_{NoC}$-L13TAG-R171C-IM.

The following plasmids were used in this study for mammalian cell culture: pBABE-puro (#1764; Addgene), pBABE-mNG-Mfn1(M.m)-puro (47) and mNeonGreen-Mfn1 (H.s) (#195162; Addgene). To create pBABE-mNG-Mfn1(H.s), the Mfn1(H.s) was inserted into the pBABE vector using Gibson assembly. pBABE-mNG-Mfn1(H.s)- NoC was created through replacing the sequence for the first 364 residues of mfn1(H.s) with the sequences for these residues from pETM11-Mfn1-C111S-C156A-C167A-C196A-C260S-C327A-IM-GSSG-TEV-TwinStrep using Gibson assembly. After digestion with DpnI to remove template DNA, the amplified DNA was transformed into Endura or DH5-α *Escherichia coli* cells and plasmids were purified from selected colonies. All plasmids were confirmed by sequence analysis.

Expression and Purification of the Mfn1-IM construct. All Mfn1-IM constructs described were co-transformed with the AcdA9 aminoacyl tRNA synthetase/tRNA-containing plasmid (pDule2) into BL21 *E. coli* cells. Cells were then cultured in Luria-Bertani medium at 37°C with 50 µg/ml kanamycin and 60 µg/ml spectinomycin to an OD600 ~0.8. Protein expression was induced by adding 0.5 mM isopropyl β-D-1-thiogalactopyranoside (IPTG) and Acd (for a final

concentration of 0.3 mM). These cultures were grown overnight (17-19 hrs) at 17.5°C. Cells were harvested by centrifugation, frozen in liquid nitrogen, and stored at -80°C. Cells were thawed with a room temperature water bath and resuspended in lysis buffer (50 mM MgCl, 30 mM Tris, 1 mM β-mercaptoethanol, 400mM NaCl, pH 7.4) supplemented with HALT protease inhibitor cocktail. Cell suspensions were lysed using Sonic Dismembrator Model 100 sonicator at power 5 for 4 seconds. This was repeated 3 times with the samples resting on ice for a minute between each cycle. The lysate was subject to centrifugation at 21,000 xg for 20 minutes. The supernatant was loaded onto 0.25 mL bed volume Strep-Tactin Superflow high-capacity beads (iba Biosciences) in a disposable gravity-flow column. The resin bound to protein was washed with 5 column volumes of wash solution (50 mM MgCl, 30 mM Tris, 1 mM β-mercaptoethanol, 400mM NaCl, pH 7.4) and eluted with 625 μM d-Desthiobiotin (Sigma) in wash buffer. Mfn1-IM-containing elutions were treated with 10 mM tris(2-carboxyethyl)phosphine (TCEP) to fully reduce cysteines. It was desalted into KMgT buffer (50mM KCl, 5mM $MgCl_2$, 30mM Tris-HCl, pH 7.4, 100uM TCEP) with a Zeba Spin Desalting Column (0.5 mL). The concentration was adjusted to 14uM and then glycerol was added to 20%, for a final concentration of 10uM, before the protein was aliquoted flash frozen with liquid nitrogen and stored at -80°C.

Cyclic Nucleotides and Labeling Reagents. Guanosine triphosphate (GTP) and guanosine 5'-diphosphate (sodium salt hydrate) (GDP) were purchased from Sigma-Aldrich. Guanosine 5'-O-[gamma-thio] triphosphate (GTPγS) and guanosine 5'-[β,γ-imido] triphosphate (GMP-PNP) were purchase from Cayman Chemical. GTP, GDP, and GTPγS were resuspended in 1M Pipes-KOH pH 7.6 at 75 mM. GMP-PNP was resuspended in 1M Pipes-KOH pH7.6 at 37.5mM. $[Cu(cyclenM)]^{2+}$ for tmFRET were prepared as previously described (32, 35).

Cell culture and transfection. All cells were grown at 37°C and 5% CO_2 and cultured in DMEM (Thermo Fisher Scientific) containing 1× GlutaMAX (Thermo Fisher Scientific) with 10% FBS (Seradigm). Mfn1-null MEF cells were purchased from the American Type Culture Collection.

Retroviral transduction. Plat-E cells (Cell Biolabs) were maintained in complete media supplemented with 1 μg/ml puromycin and 10 μg/ml blasticidin and plated at ~80% confluency the day before transfection. 350,000 Plat-E cells were plated in a six-well dish and the following day were transfected with pBABE plasmids (3 μg pBABE Mfn1 or an empty vector) using FuGENE HD (Promega) and Opti-MEM reduced serum media (Gibco). Transfection reagent was incubated overnight before a media change. Viral supernatants were collected at ~48 and 72 hr post-transfection and incubated with MEFs in the presence of 8 μg/ml polybrene. ~24 h after the last viral transduction, MEF cells were split and selection was added (1 μg/ml puromycin).

Microscopy. All cells were plated ingrown on no. 1.5 glass-bottomed dishes (MatTek) for ~48 h before imaging. Cells were incubated with 0.1 μg/ml MitoTracker Red CMXRos for 15 min at 37°C with 5% CO_2. After this, MEF cells were rinsed into complete media for at least one hour before imaging and one drop of one drop NucBlue (Molecular Probes). A Z-series with a step

size of 0.25 μm was collected with a Nikon Ti2E confocal microscope with a 60 × NA (numerical aperture) 1.4 oil objective (Nikon), a cicero spinning disk, a 5 channel Celesta light source (Nikon), and an sCMOS camera (Prime BSI Express). Each cell line was imaged on at least three separate occasions by a blinded experimenter (n > 100 cells per experiment).

Image analysis. Images were deconvolved using 15 iterations of 3D Landweber deconvolution. Deconvolved images were then analyzed using Nikon Elements software. Maximum intensity projections were created using ImageJ software (NIH). Mitochondrial morphology in mammalian cells was scored as follows: hyperfused indicates that the entire mitochondrial network in the cell was connected as a single structure; reticular indicates that fewer than 30% of the mitochondria in the cell were fragments (fragments defined as mitochondria less than 2.5 μm in length); fragmented indicates that most of the mitochondria in the cell were less than 2.5 μm in length. In MEF cells expressing mNeonGreen-Mfn1, only cells with GFP signal were scored.

TCSPC Lifetime measurements. TCSPC lifetime data of Acd labeled protein samples at 300 nM (100uL) was measured in 50 μL volume quartz cuvettes (Starna Cells, inc). Lifetime data were measured using a PicoQuant FluoTime 300 Fluorescence Lifetime Spectrometer (PicoQuant, Berlin Germany) with 375 nm UV laser excitation and 446 nm emission. Single photo arrivals were recorded on a hybrid photomultiplier detector assembly (PMA-40). Four cuvettes were consecutively recorded, the first with Mfn1-L13Acd-R171C, the second with Mfn1-L13Acd-NoC, the third with buffer-only correspondent to the buffer of each experiment, and the fourth with diluted LUDOX in MiliQ water for measurement of the instrument response function (IRF). First the lifetime of all cuvettes was recorded without the labelling of $[Cu(cyclenM)]^{2+}$. Then 1uL of 11mM $[Cu(cyclenM)]^{2+}$ was added and the lifetimes were measured until labelling was stable. This was done in the following buffer conditions:

Apo: 50 mM KCl, 5 mM $MgCl_2$, 30 mM Tris-HCl, pH 7.4
GDP: 50 mM KCl, 5 mM $MgCl_2$, 30 mM Tris-HCl, pH 7.4, 750 mM GDP
GMP-PNP: 50 mM KCl, 5 mM $MgCl_2$, 30 mM Tris-HCl, pH 7.4, 750 mM GMP-PNP
GTPγS: 50 mM KCl, 5 mM $MgCl_2$, 30 mM Tris-HCl, pH 7.4, 750 mM GTPγS
GDP•BeF_3: 50 mM KCl, 5 mM $MgCl_2$, 30 mM Tris-HCl, pH 7.4, 750 mM GDP, 25 mM NaF, 250 mM $BeSO_4$

FRET model of time-domain fluorescence lifetime data to obtain Gaussian distance distributions. Fitting is as previously described (42). Briefly:

The time-domain fluorescence lifetime data of the donor fluorophore in the presence of the acceptor were fit by model estimates for the time course of the decay, $Decay(t)$. These fits were calculated from the convolution of the measured instrument response function, $IRF(t)$ of the system with model estimates of the fluorescence lifetime of the donor in the presence of the acceptor, $I_{DA}(t)$ and buffer-only fluorescence $I_B(t)$:

$$Decay(t) = \int_{-\infty}^{\infty} \left[IRF(t' - shift_{irf}) - bkgr_{irf}\right]\left[I_{DA}(t - t') + f_B\, I_B(t - t')\right]dt' + bkgr_{dec}$$

Equation 1

Where the variables are defined in Table I and displayed graphically in Figure 8.

Table I

Variable	**Description**
t	Time of photon emission (in s)
r	Distance between the donor and acceptor (in Å)
$Decay(t)$	Time-dependent decay of the donor fluorescence (in counts)
$DecayB(t)$	Time-dependent decay of the buffer-only fluorescence (in counts)
$I_{DA}(t)$	Model estimate of the fluorescence lifetime of the donor in the presence of the acceptor (in counts)
$I_B(t)$	Model estimate of the fluorescence lifetime of a buffer-only sample (in counts)
$IRF(t)$	Measured instrument response function (in counts)
$bkgr_{dec}$	Time-independent decay background (in counts)
$bkgr_{irf}$	Time-independent background of the instrument response function (in counts)
$shift_{irf}$	Time shift between the instrument response function and the measured decay (in ps)
f_B	Scaling of the buffer fluorescence
A_0	Amplitude of the model estimate of the fluorescence lifetime of the donor (in counts)
f_D	Fraction of donor-only fluorescence in the sample
α_{Di}	Fraction of the ith component of the donor-only fluorescence (in counts)
τ_{Di}	Time constant of the ith component of the donor-only fluorescence (in s)
α_{Bi}	Amplitude of the ith component of the buffer fluorescence (in counts)
τ_{Bi}	Time constant of the ith component of the buffer fluorescence (in s)
R_0	Characteristic distance between donor and acceptor producing 50% FRET efficiency
$\rho(r)$	Probability distance distribution of the donor and acceptor distances
f_{Ai}	Fraction of the ith component of the probability distance distribution

$\bar{r}_i$	Average distance of the ith component of the donor-only fluorescence (in Å)
σ_i	Standard deviation of the ith component of the donor-only fluorescence (in Å)

The model for fluorescence lifetime assumes a donor-only fluorescence lifetime with one or two exponential components, and FRET between a donor and acceptor separated by one or two Gaussian-distributed distances, similar to that previously described for frequency domain measurements (9, 18, 21, 34). This model predicts the following relationship for the fluorescence lifetime of the donor in the presence of acceptor, $I_{DA}(t)$:

$$I_{DA}(t) = A_0 \left[f_D \sum_{i=1}^{2} \alpha_{Di}\, e^{\left(-\frac{t}{\tau_{Di}}\right)} + (1 - f_D) \int_0^{\infty} \rho(r) \sum_{i=1}^{2} \alpha_{Di}\, e^{\left[-\frac{t}{\tau_{Di}} - \frac{t}{\tau_{Di}}\left(\frac{R_0}{r}\right)^6\right]} dr \right] \qquad \text{Equation 2}$$

Where $\alpha_{D1} + \alpha_{D2} = 1$.

The density distribution of donor-acceptor distances, $\rho(r)$, was assumed to be the sum of up to two Gaussians:

$$\rho(r) = \sum_{i=1}^{2} f_{Ai} \frac{1}{\sigma_i \sqrt{2\pi}}\, e^{\left[-\frac{1}{2}\left(\frac{r-\bar{r}_i}{\sigma_i}\right)^2\right]} \qquad \text{Equation 3}$$

where $f_{A1} + f_{A2} = 1$.

The decay time course of the buffer-only sample, $DecayB(t)$, was fit with a convolution of the measured instrument response function, $IRF(t)$ with a multi-exponential model for the fluorescence lifetime, $I_B(t)$:

$$DecayB(t) = \int_{-\infty}^{\infty} \left[IRF(t' - shift_{irf}) - bkgr_{irf}\right] [I_B(t - t')] dt' + bkgr_{dec} \qquad \text{Equation 4}$$

$$I_B(t) = \sum_{i=1}^{4} \alpha_{Bi}\, e^{\left(-\frac{t}{\tau_{Bi}}\right)} \qquad \text{Equation 5}$$

This model for the buffer-only fluorescence lifetime was then added to the model for the sample lifetime before convolving with the $IRF(t)$ (Equation 1).

This FRET model for fluorescence lifetimes and FRET was implemented in Igor Pro v8 (Wavemetrics, Lake Oswego, OR) (code available at https://github.com/zagotta/TDlifetime_program). The FRET model was either fit, with χ^2 minimization, assuming a standard deviation equal to $\sqrt{Decay(t)}$, to individual decay time courses, or globally fit to multiple decays with the sample under different conditions as indicated in the text. There are 15 parameters in the parameter vector $(f_D, \tau_{D1}, \alpha_{D1}, \tau_{D2},\ R_0, \bar{r}_1, \sigma_1, f_{A2}, \bar{r}_2, \sigma_2, shift_{irf}, f_B, A_0, bkgr_{dec}, bkgr_{irf})$. R_0 was fixed to a

value previously determined from emission spectra of the donor and absorbance spectra of the acceptor using the Förster equation assuming $\kappa^2 = 2/3$. f_{A2},was generally fixed to 0 or 1 for fits assuming a single Gaussian distance distribution but was allowed to vary when multiple distance components were expected (e.g. with subsaturating ligand concentrations). f_B was fixed to the acquisition time for the experimental sample divided by the acquisition time for the buffer-only sample. And $bkgr_{irf}$was always fixed to 0 as the average background photon count in the $IRF(t)$ was <<1.

For the individual decay fits to the donor-only sample, f_D was set to 1, and only $\tau_{D1}, \alpha_{D1}, \tau_{D2}, shift_{irf}, A_0, bkgr_{dec}$ were allowed to vary. For the individual decay fits to the donor+acceptor samples, $\tau_{D1}, \alpha_{D1}, \tau_{D2}$were constrained to the previously determined values from the donor-only sample, and $f_D, \bar{r}_1, \sigma_1, f_{A2}, \bar{r}_2, \sigma_2, shift_{irf}, A_0, bkgr_{dec}$ were varied.

Acknowledgements

We thank the Oregon State University GCE4ALL (Center for Genetic Code Expansion for All) for their long-standing collaboration and Dr. Pierce Eggan, Charlie DeFreest, Dr. Shauna Otto, and Dr. Stephanie Sloat for technical support and scientific discussions. Funding was provided by grants from the National Institute of General Medical Sciences (R01GM118509 to SH; TGGM153507 to SMH; R35GM145225 to SEG; R35GM148137 to WNZ).

Literature cited

1. A. N. Hutson, K. Rochon, J. A. Mears, Conformational Rearrangement of Fission DSPs. *BioEssays* **n/a**, e70062.
2. H. Khurana, T. J. Pucadyil, "Gearing" up for dynamin-catalyzed membrane fission. *Current Opinion in Cell Biology* **83**, 102204 (2023).
3. R. Kalia, A. Frost, Open and cut: allosteric motion and membrane fission by dynamin superfamily proteins. *Mol Biol Cell* **30**, 2097–2104 (2019).
4. J. R. Jimah, J. E. Hinshaw, Structural Insights into the Mechanism of Dynamin Superfamily Proteins. *Trends Cell Biol* **29**, 257–273 (2019).
5. S. C. J. Helle, *et al.*, Mechanical force induces mitochondrial fission. *eLife* **6**, e30292 (2017).
6. H. Alimohamadi, *et al.*, Dynamin-like Proteins Combine Mechano-constriction and Membrane Remodeling to Enable Two-Step Mitochondrial Fission via a "Snap-through" Instability. *J. Am. Chem. Soc.* **147**, 24258–24274 (2025).
7. J. S. Chappie, *et al.*, A pseudoatomic model of the dynamin polymer identifies a hydrolysis-dependent powerstroke. *Cell* **147**, 209–222 (2011).
8. J. S. Chappie, F. Dyda, Building a fission machine--structural insights into dynamin assembly and activation. *J Cell Sci* **126**, 2773–2784 (2013).

9. E. Cocucci, R. Gaudin, T. Kirchhausen, Dynamin recruitment and membrane scission at the neck of a clathrin-coated pit. *MBoC* **25**, 3595–3609 (2014).
10. S. Hoppins, *et al.*, The soluble form of Bax regulates mitochondrial fusion via MFN2 homotypic complexes. *Mol Cell* **41**, 150–160 (2011).
11. H. Chen, *et al.*, Mitofusins Mfn1 and Mfn2 coordinately regulate mitochondrial fusion and are essential for embryonic development. *J Cell Biol* **160**, 189–200 (2003).
12. A. Santel, *et al.*, Mitofusin-1 protein is a generally expressed mediator of mitochondrial fusion in mammalian cells. *J Cell Sci* **116**, 2763–2774 (2003).
13. L. Tilokani, S. Nagashima, V. Paupe, J. Prudent, Mitochondrial dynamics: overview of molecular mechanisms. *Essays Biochem* **62**, 341–360 (2018).
14. L.-C. Tábara, M. Segawa, J. Prudent, Molecular mechanisms of mitochondrial dynamics. *Nat Rev Mol Cell Biol* **26**, 123–146 (2025).
15. S. Mattie, M. Krols, H. M. McBride, The enigma of an interconnected mitochondrial reticulum: new insights into mitochondrial fusion. *Curr Opin Cell Biol* **59**, 159–166 (2019).
16. A. Suomalainen, J. Nunnari, Mitochondria at the crossroads of health and disease. *Cell* **187**, 2601–2627 (2024).
17. R. Quintana-Cabrera, L. Scorrano, Determinants and outcomes of mitochondrial dynamics. *Mol Cell* **83**, 857–876 (2023).
18. G. W. Dorn, Evolving Concepts of Mitochondrial Dynamics. *Annu Rev Physiol* **81**, 1–17 (2019).
19. S. Züchner, *et al.*, Mutations in the mitochondrial GTPase mitofusin 2 cause Charcot-Marie-Tooth neuropathy type 2A. *Nat Genet* **36**, 449–451 (2004).
20. S. M. E. Feely, *et al.*, MFN2 mutations cause severe phenotypes in most patients with CMT2A. *Neurology* **76**, 1690–1696 (2011).
21. C. Alberti, *et al.*, Charcot-Marie-tooth disease type 2A: An update on pathogenesis and therapeutic perspectives. *Neurobiol Dis* **193**, 106467 (2024).
22. P. J. Flannery, E. Trushina, Mitochondrial Dynamics and Transport in Alzheimer's Disease. *Mol Cell Neurosci* **98**, 109–120 (2019).
23. V. M. Pozo Devoto, T. L. Falzone, Mitochondrial dynamics in Parkinson's disease: a role for α-synuclein? *Dis Model Mech* **10**, 1075–1087 (2017).
24. V. S. Van Laar, S. B. Berman, Mitochondrial dynamics in Parkinson's disease. *Exp Neurol* **218**, 247–256 (2009).
25. E. Abati, *et al.*, Investigating the prevalence of MFN2 mutations in amyotrophic lateral sclerosis: insights from an Italian cohort. *Brain Commun* **6**, fcae312 (2024).
26. O. Daumke, A. Roux, Mitochondrial Homeostasis: How Do Dimers of Mitofusins Mediate Mitochondrial Fusion? *Curr Biol* **27**, R353–R356 (2017).
27. Y.-L. Cao, *et al.*, MFN1 structures reveal nucleotide-triggered dimerization critical for mitochondrial fusion. *Nature* **542**, 372–376 (2017).
28. Y. Qi, *et al.*, Structures of human mitofusin 1 provide insight into mitochondrial tethering. *J Cell Biol* **215**, 621–629 (2016).
29. L. Yan, *et al.*, Structural basis for GTP hydrolysis and conformational change of MFN1 in mediating membrane fusion. *Nat Struct Mol Biol* **25**, 233–243 (2018).
30. Y.-J. Li, *et al.*, Structural insights of human mitofusin-2 into mitochondrial fusion and CMT2A onset. *Nat Commun* **10**, 4914 (2019).
31. T. Koshiba, *et al.*, Structural basis of mitochondrial tethering by mitofusin complexes. *Science* **305**, 858–862 (2004).

32. W. N. Zagotta, *et al.*, An improved fluorescent noncanonical amino acid for measuring conformational distributions using time-resolved transition metal ion FRET. *Elife* **10**, e70236 (2021).
33. L. C. Speight, *et al.*, Efficient Synthesis and In Vivo Incorporation of Acridon-2-ylalanine, a Fluorescent Amino Acid for Lifetime and FRET/LRET Studies. *J Am Chem Soc* **135**, 18806–18814 (2013).
34. J. S. Mortensen, C. J. Loland, Short-Range Distance Measurement by Transition Metal Ion FRET. *Methods Mol Biol* **2168**, 299–311 (2020).
35. S. E. Gordon, E. N. Senning, T. K. Aman, W. N. Zagotta, Transition metal ion FRET to measure short-range distances at the intracellular surface of the plasma membrane. *J Gen Physiol* **147**, 189–200 (2016).
36. J. R. Lakowicz, Ed., *Principles of Fluorescence Spectroscopy* (Springer US, 2006).
37. H. H. Low, C. Sachse, L. A. Amos, J. Löwe, Structure of a bacterial dynamin-like protein lipid tube provides a mechanism for assembly and membrane curving. *Cell* **139**, 1342–1352 (2009).
38. S. Mattie, J. Riemer, J. G. Wideman, H. M. McBride, A new mitofusin topology places the redox-regulated C terminus in the mitochondrial intermembrane space. *J Cell Biol* **217**, 507–515 (2018).
39. E. A. Engelhart, S. Hoppins, A catalytic domain variant of mitofusin requiring a wildtype paralog for function uncouples mitochondrial outer-membrane tethering and fusion. *J Biol Chem* **294**, 8001–8014 (2019).
40. S. R. Sloat, B. N. Whitley, E. A. Engelhart, S. Hoppins, Identification of a mitofusin specificity region that confers unique activities to Mfn1 and Mfn2. *Mol Biol Cell* **30**, 2309–2319 (2019).
41. P. Eggan, S. E. Gordon, W. N. Zagotta, Ligand-coupled conformational changes in a cyclic nucleotide-gated ion channel revealed by time-resolved transition metal ion FRET. *Elife* **13**, RP99854 (2024).
42. P. Eggan, S. E. Gordon, W. N. Zagotta, Domain coupling in allosteric regulation of SthK measured using time-resolved transition metal ion FRET. *Elife* **14**, RP106892 (2025).
43. W. N. Zagotta, *et al.*, Measuring conformational equilibria in allosteric proteins with time-resolved tmFRET. *Biophys J* **123**, 2050–2062 (2024).
44. M. H. Tessmer, S. Stoll, chiLife: An open-source Python package for in silico spin labeling and integrative protein modeling. *PLoS Comput Biol* **19**, e1010834 (2023).
45. L. J. Byrnes, H. Sondermann, Structural basis for the nucleotide-dependent dimerization of the large G protein atlastin-1/SPG3A. *Proc Natl Acad Sci U S A* **108**, 2216–2221 (2011).
46. L. Shi, *et al.*, Dissecting the mechanism of atlastin-mediated homotypic membrane fusion at the single-molecule level. *Nat Commun* **15**, 2488 (2024).
47. S. R. Sloat, S. Hoppins, A dominant negative mitofusin causes mitochondrial perinuclear clusters because of aberrant tethering. *Life Sci Alliance* **6**, e202101305 (2023).

Figure Legends

Figure 1 The catalytic cycle drives conformational changes in Mfn1 (A, left) Schematic of Mfn1 functional states linked to the nucleotide-bound state and function throughout the catalytic cycle. At the top left, Mfn1 is bound to GTP, which permits formation of the tethering complex. Hydrolysis of GTP results in GDP+Pi in the nucleotide binding pocket and is theorized to be the driving force to bring the opposing membrane together. The release of Pi results in the GDP bound state, which could be when lipids mixing occurs. Lastly, GDP is released and Mfn1 is bound to no nucleotide. **(A, right)** A schematic denoting the domains found in mitofusin. Black lines below indicate the domains in the crystallization constructs, referred to as mini-mitofusin. The mini-Mfn1 dimers containing the GTPase, Hinge2, and HB1 domains. As observed in other DSPs, an intermolecular interface between GTPase domains is essential for GTP hydrolysis (G-G interface). The closed conformation was observed with mini-Mfn1 bound to GDP•BeF_3, replicating GDP+Pi (Bottom), while the open conformation is mini-Mfn1 bound to GDP (Top). **(B)** Schematic of tmFRET with Acd incorporated into the protein and the transition metal ion bound to a cysteine via cyclen-maleimide. Acd is excited at 372 nm and emission is recorded at 446 nm. Fluorescence is quenched by the metal acceptor with an efficiency that is highly dependent on distance. **(C)** Theoretical fluorescence lifetime decays of a donor fluorophore in the time-domain showing basis of time-resolved tmFRET. A single exponential donor (short and long) and population of tmFRET distances are shown.

Figure 2 Development of tmFRET donor-acceptor pair on mini-Mfn1. (A) GTPase activity of 5 μM mini-Mfn1 or mini-Mfn1-NoC was measured with a malachite green assay. **(B)** Representative live cell images of Mfn1-null MEF cells with empty vector or expressing the indicated mNeonGreen-Mfn1 construct (mNG-Mfn1)(M.m: *Mus musculus*; Hs: *Homo sapiens*). Mitochondria were labeled with Mitotracker Red CMXRos and nuclei were labeled with NucBlue and both were visualized by fluorescence microscopy. **(C)** Quantification of mitochondrial morphology for cell lines described in (B). The error bars represent the standard deviation of the five independent and blinded experiments. **(D)** Coomassie gel staining (left) and in-gel fluorescence (right) of different fractions from Twin-strep mini-Mfn1-L13Acd purification (Lysate [L], Flowthrough [FT], Wash 1 [W1], Elution 1-4 [E1-4]). **(E)** Coomassie gel staining of different fractions from Twin-strep mini-Mfn1-L13Acd-R171C purification as in D. **(F)** GTPase activity of 5 μM mini-Mfn1-WT or mini-Mfn1-L13Acd-R171C were measured with a malachite green assay.

Figure 3 Steady-state lifetime tmFRET of mini-Mfn1 in the GDP-bound and transition states. (**A**) Cartoon structure of mini-Mfn1 in the GDP-bound state with the predicted rotameter states of L13Acd (green) and R171[Cu(cyclenM)]$^{2+}$ (purple) with an average predicted distance of 13.7 Å. (**B**) Representative TCSPC data from saturating GDP conditions with either donor only (Mfn1-L13Acd-NoC) before (brown) and after (violet) the addition of [Cu(cyclenM)]$^{2+}$ or from mini-Mfn1-L13Acd-R171C before (grey) and after (magenta) the addition of

[Cu(cyclenM)]$^{2+}$. (**C**) Spaghetti plot of distributions from individual experiments with GDP with average of all experiments in bold, and the distribution predicted by chiLife in the dashed black curve. (**D**) Cartoon structure of mini-Mfn1 in the transition state (GDP•BeF_3) with the predicted rotameter states of L13Acd (green) and R171[Cu(cyclenM)]$^{2+}$ (purple) with an average predicted distance of 24.4 Å. (**E**) Representative TCSPC data from saturating conditions of GDP•BeF_3 with either donor only (Mfn1-L13Acd-NoC) before (brown) and after (violet) the addition of [Cu(cyclenM)]$^{2+}$ or Mfn1-L13Acd-R171C before (grey) and after (blue) the addition of [Cu(cyclenM)]$^{2+}$. (**F**) Spaghetti plot of distributions from individual experiments with GDP•BeF_3 fit to a single Gaussian with the average of all experiments in bold, and the distribution predicted by chiLife in the dashed black curve. (**G**) Spaghetti plot of distributions from individual experiments with GDP•BeF_3 fit to a dual Gaussian with the average in bold (blue). The GDP•BeF_3-bound state distribution predicted by chiLife (dashed black curve) and the experimental average GDP distribution dashed magenta curve) are overlayed.

Figure 4 Steady-state lifetime tmFRET of mini-Mfn1- R73A in the transition- and GDP-bound states. (**A**) Representative TCSPC data from saturating GDP conditions with either donor only (Mfn1-L13Acd-R73Q-NoC) after (violet) the addition of [Cu(cyclenM)]$^{2+}$ or from mini-Mfn1-L13Acd-R73Q-R171C before (grey) and after (magenta) the addition of [Cu(cyclenM)]$^{2+}$. (**C**) Spaghetti plot of distributions from individual experiments with GDP. Average is in bold, and wild-type distribution shown in the dashed black curve. (**C**) Representative TCSPC data from saturating conditions of GDP•BeF_3 with either donor only (Mfn1-L13Acd-R73Q-NoC) after (violet) the addition of [Cu(cyclenM)]$^{2+}$ or Mfn1-L13Acd-R73Q-R171C before (grey) and after (blue) the addition of [Cu(cyclenM)]$^{2+}$. (**D**) Spaghetti plot of distributions from individual experiments with GDP•BeF_3 with the average in bold, and distribution predicted by chiLife shown in the dashed black curve. (**E**) Spaghetti plot of distributions from Mfn1-L13Acd-R73Q-R171C in GDP•BeF_3 (black) compared to wildtype in GDP (magenta) and GDP•BeF_3 (blue), illustrating the R73Q variant does not access the wild-type GDP•BeF_3 state.

Figure 5 Steady-state lifetime tmFRET of mini-Mfn1 with GTPyS or GMP-PNP bound. (**A**) Representative TCSPC data from saturating GTPyS conditions with either donor only (Mfn1-L13Acd-NoC) after (violet) the addition of [Cu(cyclenM)]$^{2+}$ or from mini-Mfn1-L13Acd-R171C before (grey) and after (cyan) the addition of [Cu(cyclenM)]$^{2+}$. (**B**) Spaghetti plot of distributions from individual experiments with GTPyS. Average is in displayed in bold. (**C**) Representative TCSPC data from saturating GMP-PNP conditions with either donor only (Mfn1-L13Acd-NoC) after (violet) the addition of [Cu(cyclenM)]$^{2+}$ or from mini-Mfn1-L13Acd-R171C before (grey) and after (green) the addition of [Cu(cyclenM)]$^{2+}$ (**D**) Spaghetti plot of distributions from individual experiments with GMP-PNP. Average wave is displayed in bold. (**E**) Spaghetti plot of average distributions for GTPyS (cyan), GDP (magenta), and GMP-PNP (green).

Figure 6 Steady-state lifetime tmFRET of mini-Mfn1 in the apo state. (**A**) Representative TCSPC data with either donor only (Mfn1-L13Acd-NoC) after (violet) the addition of

$[Cu(cyclenM)]^{2+}$ or from mini-Mfn1-L13Acd-R171C before (grey) and after (orange) the addition of $[Cu(cyclenM)]^{2+}$ (**B**) Spaghetti plot of distributions from individual experiments with no nucleotide bound. The average distribution is displayed in bold. (**C**) Spaghetti plot of average distributions for GDP (magenta) and apo (orange) **(D)** Mean distances for individual experiments in the presence of GDP or no nucleotide, identifying a statistical difference between the conditions. **(E)** Sigma for individual experiments when in the presence of GDP or no nucleotide, identifying a statistical difference between the conditions.

Figure 7 A model for the conformational changes driven by the catalytic cycle of Mfn1. Our data demonstrate that the GTPase and HB1 domains are in the open state for GTP-Mfn1, which supports membrane tethering. GTP hydrolysis results in GDP+Pi in the binding pocket and our data indicate an equilibrium between open and closed, with the closed state favored. Release of Pi results in GDP-Mfn1, which is in the open state. When GDP is released and Mfn1 is in the apo state, our data indicate that the GTPase domain and HB1 are in unique positions compared to the other states.

Supplemental Figure Legends

Supplemental Figure 1: Acd Incorporation at L13 of mini-Mfn1. (A) Mass spectrometry analysis of mini-Mfn1-NoC to get the predominate product off the column of 51015.0 Da, which agrees with the mass of the mini-Mfn1-NoC construct without the initial methionine, which is commonly separated during mass spectrometry. There are no other comparable peaks, demonstrating a clean purification**. (B)** Mass Spectrometry analysis of mini-Mfn1-L13Acd-NoC to get the predominate product of 51166.0 Da. This demonstrates a change in 151 Da from Acd incorporation, which only arises from a leucine being substituted for Acd. The absence of other comparable peaks demonstrates specific integration.

Supplemental Figure 2: Mfn1-L13Acd-R238A-R171C does not alter conformations throughout GTP hydrolysis (**A**) Representative TCSPC data from Mfn1-L13Acd-R238A-NoC in the presence of $[Cu(cyclenM)]^{2+}$(violet) and Mfn1-L13Acd-R238A R171C before (grey) and after (orange) the addition of $[Cu(cyclenM)]^{2+}$. (**B**) Spaghetti plot of distributions from individual experiments with no nucleotide bound with the average of the waves displayed in bold. (**C**) Spaghetti plot of distributions from individual experiments with GMP-PNP bound with the average of the waves displayed in bold. (**D**) Spaghetti plot of distributions from individual experiments with GDP bound with the average of the waves displayed in bold. (**E**) Spaghetti plot of distributions from individual experiments with GDP•BeF_3 bound with the average of the waves displayed in bold. (**E**) Spaghetti plot of average wave distributions for apo (orange), GMP-PNP (green), GDP (magenta) GDP•BeF_3 (blue), and apo-WT-Mfn1 (black).

Supplemental Figure 3. Parameters used in the FRET model, shown in blue, for TCSPC data for the sum of two Gaussians distribution. (A) Graph of donor-only fluorescence-lifetime

decay with two exponential components with time constants (τ_{D1}, τ_{D2}). The amplitude fraction of the donor-only lifetime in an experiment is determined as f_D. (**B)** FRET efficiency (*E*) plot as a function of distance (*r*) between donor and acceptor and the R_0 values for 50% FRET transfer. **(C)** Probability distribution plot of donor and acceptor distances P(*r*) showing the sum of two Gaussian distributions, each with their own average distance ($\overline{r_1}$ and $\overline{r_2}$), standard deviations (σ_1 and σ_2) and relative amplitude of the second component (f_{A2}). **(D)** Example TCSPC data is shown with experimental measured photon count data (Decay), the instrument response function (IRF), and the buffer only decay (DecayB), with its corresponding scaling factor f_B relative to the Decay trace. Also indicated is a time-independent background of photon counts for the Decay trace, $bkgr_{dec}$, as well as two parameters associated with the IRF, its background, $bkgr_{irf}$, and the shift between instrument response function and measured decay, $shift_{irf}$. Parameter A_0 is the amplitude of the FRET model estimate of the fluorescence lifetime of the donor (in photon counts).

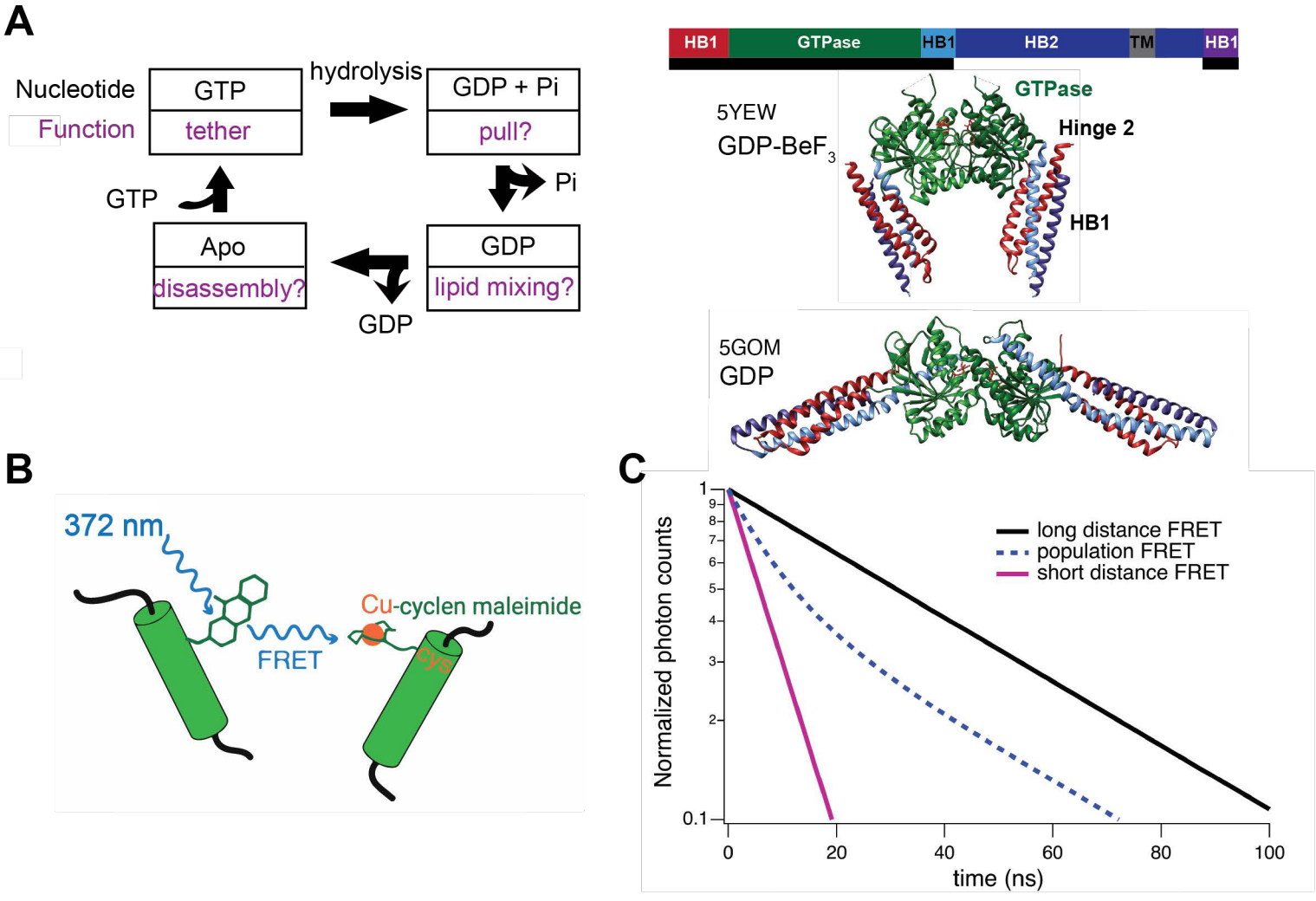

Figure 1 The catalytic cycle drives conformational changes in Mfn1 (A, left) Schematic of Mfn1 functional states linked to the nucleotide-bound state and function throughout the catalytic cycle. At the top left, Mfn1 is bound to GTP, which permits formation of the tethering complex. Hydrolysis of GTP results in GDP +Pi in the nucleotide binding pocket and is theorized to be the driving force to bring the opposing membrane together. The release of Pi results in the GDP bound state, which could be when lipids mixing occurs. Lastly, GDP is released and Mfn1 is bound to no nucleotide. **(A, right)** A schematic denoting the domains found in mitofusin. Black lines below indicate the domains in the crystallization constructs, referred to as mini-mitofusin. The mini-Mfn1 dimers containing the GTPase, Hinge2, and HB1 domains. As observed in other DSPs, an intermolecular interface between GTPase domains is essential for GTP hydrolysis (G-G interface). The closed conformation was observed with mini-Mfn1 bound to GDP•BeF3, replicating GDP + Pi (Bottom), while the open conformation is mini-Mfn1 bound to GDP (Top). **(B)** Schematic of tmFRET with Acd incorporated into the protein and the transition metal ion bound to a cysteine via cyclen-maleimide. Acd is excited at 372 nm and emission is recorded at 446 nm. Fluorescence is quenched by the metal acceptor with an efficiency that is highly dependent on distance. **(C)** Theoretical fluorescence lifetime decays of a donor fluorophore in the time-domain showing basis of time-resolved tmFRET. A single exponential donor (short and long) and population of tmFRET distances are shown.

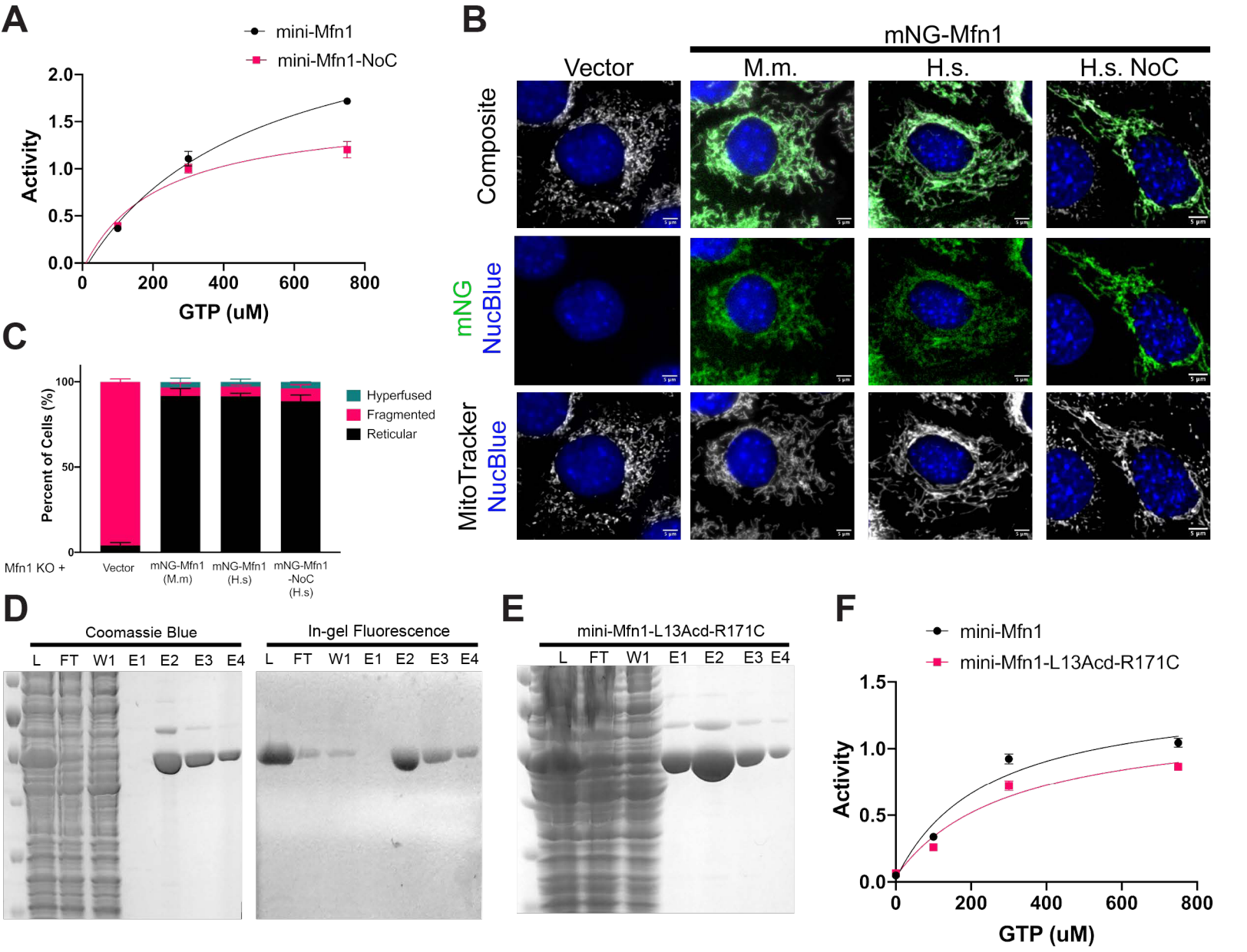

Figure 2 Development of tmFRET donor-acceptor pair on mini-Mfn1. (A) GTPase activity of 5 μM mini-Mfn1 or mini-Mfn1-NoC was measured with a malachite green assay. **(B)** Representative live cell images of Mfn1-null MEF cells with empty vector, or expressing the indicated mNeonGreen-Mfn1 construct (mNG-Mfn1)(M.m: Mus musculus; Hs: Homo sapien). Mitochondria were labeled with Mitotracker Red CMXRos and nuclei were labeled with NucBlue and both were visualized by fluorescence microscopy. **(C)** Quantification of mitochondrial morphology for cell lines described in (B). The error bars represent the standard deviation of the five independent and blinded experiments. **(D)** Coomassie gel staining (left) and in-gel fluorescence (right) of different fractions from Twin-strep mini-Mfn1-L13Acd purification (Lysate [L], Flowthrough [FT], Wash 1 [W1], Elution 1-4 [E1-4]). **(E)** Coomassie gel staining of different fractions from Twin-strep mini-Mfn1-L13Acd-R171C purification as in D. **(F)** GTPase activity of 5 μM mini-Mfn1-WT or mini-Mfn1-L13Acd-R171C were measured with a malachite green assay.

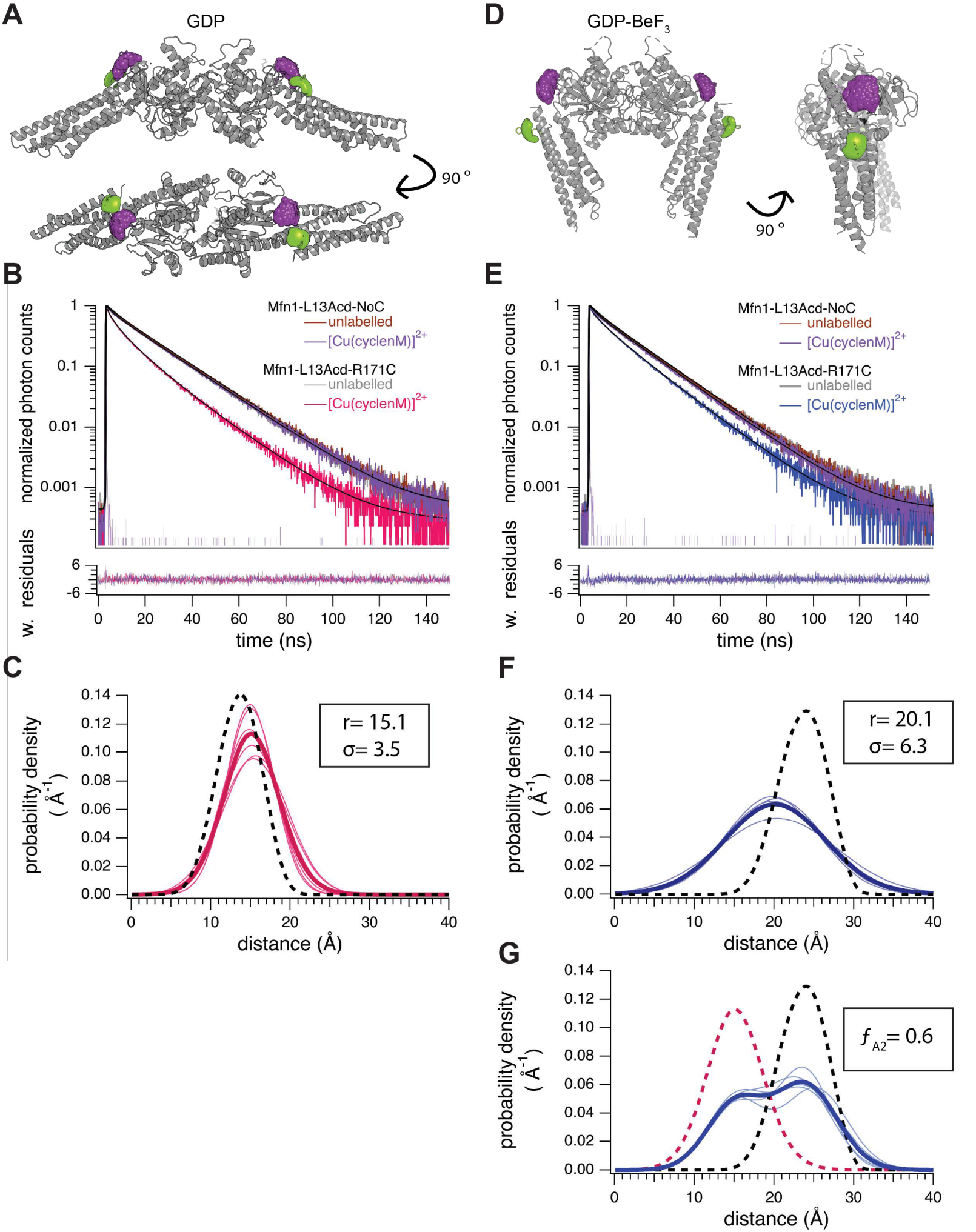
A
GDP
90 °
D
GDP-BeF3
90 °
B
Mfn1-L13Acd-NoC
unlabelled
[Cu(cyclenM)]2+
Mfn1-L13Acd-R171C
unlabelled
[Cu(cyclenM)]2+
normalized photon counts
w. residuals
time (ns)
E
Mfn1-L13Acd-NoC
unlabelled
[Cu(cyclenM)]2+
Mfn1-L13Acd-R171C
unlabelled
[Cu(cyclenM)]2+
normalized photon counts
w. residuals
time (ns)
C
r= 15.1
σ= 3.5
probability density (Å-1)
distance (Å)
F
r= 20.1
σ= 6.3
probability density (Å-1)
distance (Å)
G
fA2= 0.6
probability density (Å-1)
distance (Å)

Figure 3 Steady-state lifetime tmFRET of mini-Mfn1 in the GDP-bound and transition states. (A) Cartoon structure of mini-Mfn1 in the GDP-bound state with the predicted rotameter states of L13Acd (green) and R171[Cu(cyclenM)]$^{2+}$ (purple) with an average predicted distance of 13.7 Å. **(B)** Representative TCSPC data from saturating GDP conditions with either donor only (Mfn1-L13Acd-NoC) before (brown) and after (violet) the addition of [Cu(cyclenM)]$^{2+}$ or from mini-Mfn1-L13Acd-R171C before (grey) and after (magenta) the addition of [Cu(cyclenM)]$^{2+}$. **(C)** Spaghetti plot of distributions from individual experiments with GDP with average of all experiments in bold, and the distribution predicted by chiLife in the dashed black curve. **(D)** Cartoon structure of mini-Mfn1 in the transition state (GDP•BeF3) with the predicted rotameter states of L13Acd (green) and R171[Cu(cyclenM)]$^{2+}$ (purple) with an average predicted distance of 24.4 Å. **(E)** Representative TCSPC data from saturating conditions of GDP•BeF_3 with either donor only (Mfn1-L13Acd-NoC) before (brown) and after (violet) the addition of [Cu(cyclenM)]$^{2+}$ or Mfn1-L13Acd-R171C before (grey) and after (blue) the addition of [Cu(cyclenM)]$^{2+}$. **(F)** Spaghetti plot of distributions from individual experiments with GDP•BeF_3 fit to a single Gaussian with the average of all experiments in bold, and the distribution predicted by chiLife in the dashed black curve. **(G)** Spaghetti plot of distributions from individual experiments with GDP•BeF_3 fit to a dual Gaussian with the average in bold (blue). The GDP•BeF_3-bound state distribution predicted by chiLife (dashed black curve) and the experimental average GDP distribution dashed magenta curve) are overlayed.

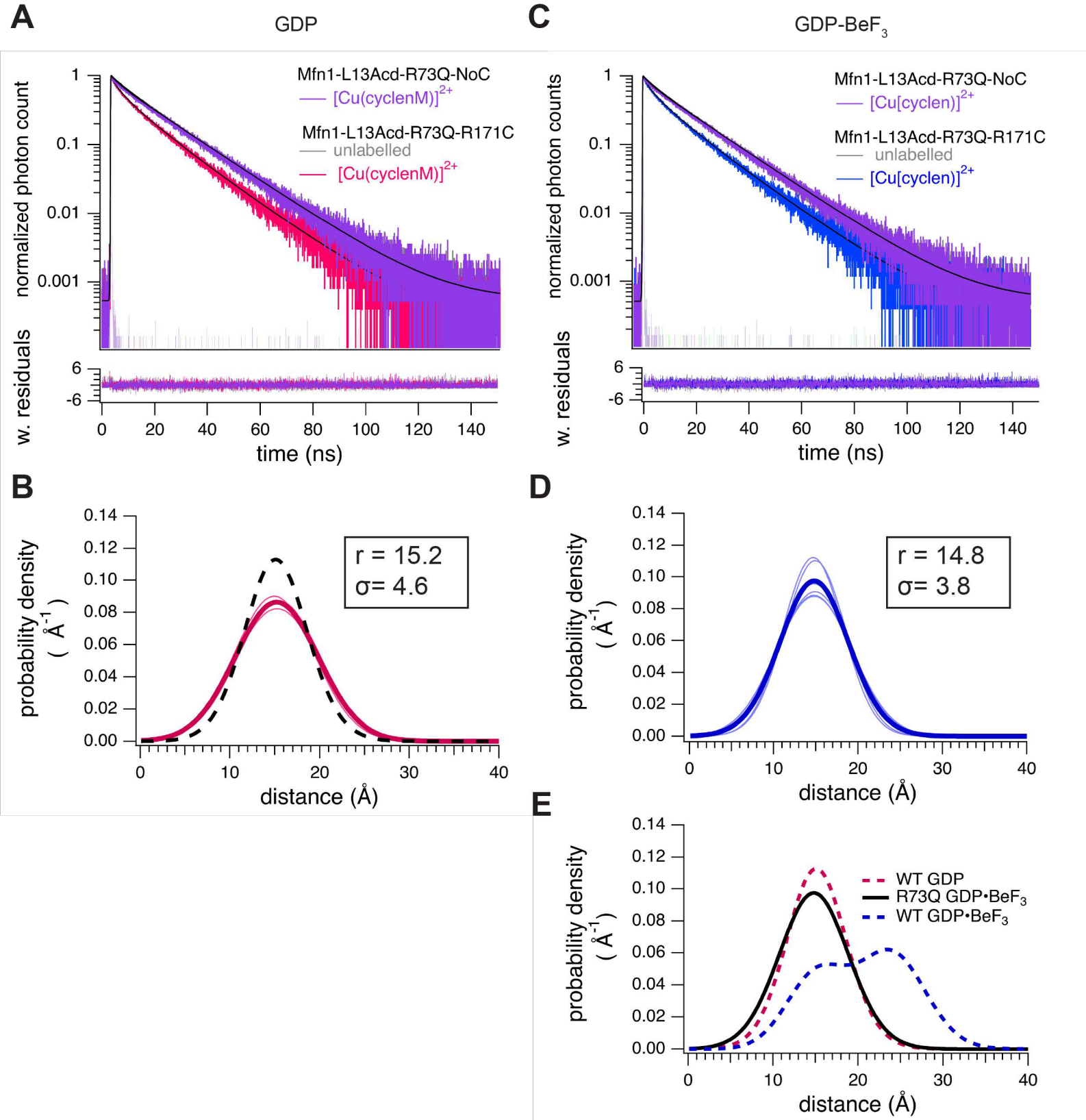

Figure 4 Steady-state lifetime tmFRET of mini-Mfn1- R73A in the transition- and GDP-bound states. (A) Representative TCSPC data from saturating GDP conditions with either donor only (Mfn1-L13Acd-R73Q-NoC) after (violet) the addition of $[Cu(cyclenM)]^{2+}$ or from mini-Mfn1-L13Acd-R73Q-R171C before (grey) and after (magenta) the addition of $[Cu(cyclenM)]^{2+}$. **(C)** Spaghetti plot of distributions from individual experiments with GDP. Average is in bold, and wildtype distribution shown in the dashed black curve. **(C)** Representative TCSPC data from saturating conditions of GDP•BeF_3 with either donor only (Mfn1-L13Acd-R73Q-NoC) after (violet) the addition of $[Cu(cyclenM)]^{2+}$ or Mfn1-L13Acd-R73Q-R171C before (grey) and after (blue) the addition of $[Cu(cyclenM)]^{2+}$. **(D)** Spaghetti plot of distributions from individual experiments with GDP•BeF_3 with the average in bold, and distribution predicted by chiLife shown in the dashed black curve. **(E)** Spaghetti plot of distributions from Mfn1-L13Acd-R73Q-R171C in GDP•BeF3 (black) compared to wildtype in GDP (magenta) and GDP•BeF3 (blue), illustrating the R73Q variant does not access the wild-type GDP•BeF_3 state.

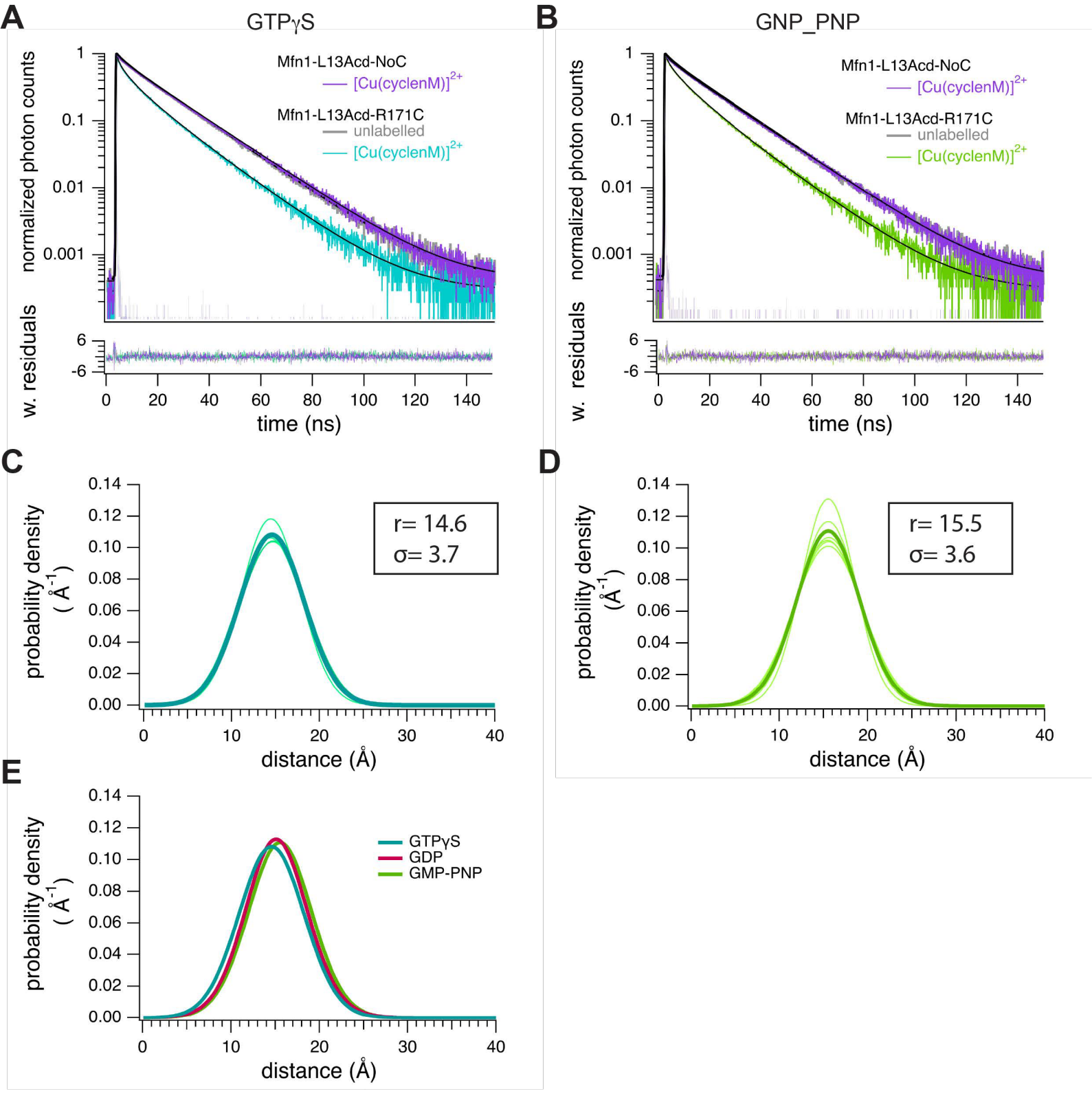

Figure 5 Steady-state lifetime tmFRET of mini-Mfn1 with GTPγS or GMP-PNP bound. (A) Representative TCSPC data from saturating GTPγS conditions with either donor only (Mfn1-L13Acd-NoC) after (violet) the addition of $[Cu(cyclenM)]^{2+}$ or from mini-Mfn1-L13Acd-R171C before (grey) and after (cyan) the addition of $[Cu(cyclenM)]^{2+}$. **(B)** Spaghetti plot of distributions from individual experiments with GTPγS. Average is in displayed in bold. **(C)** Representative TCSPC data from saturating GMP-PNP conditions with either donor only (Mfn1-L13Acd-NoC) after (violet) the addition of $[Cu(cyclenM)]^{2+}$ or from mini-Mfn1-L13Acd-R171C before (grey) and after (green) the addition of $[Cu(cyclenM)]^{2+}$ **(D)** Spaghetti plot of distributions from individual experiments with GMP-PNP. Average wave is displayed in bold. **(E)** Spaghetti plot of average distributions for GTPγS (cyan), GDP (magenta), and GMP-PNP (green).

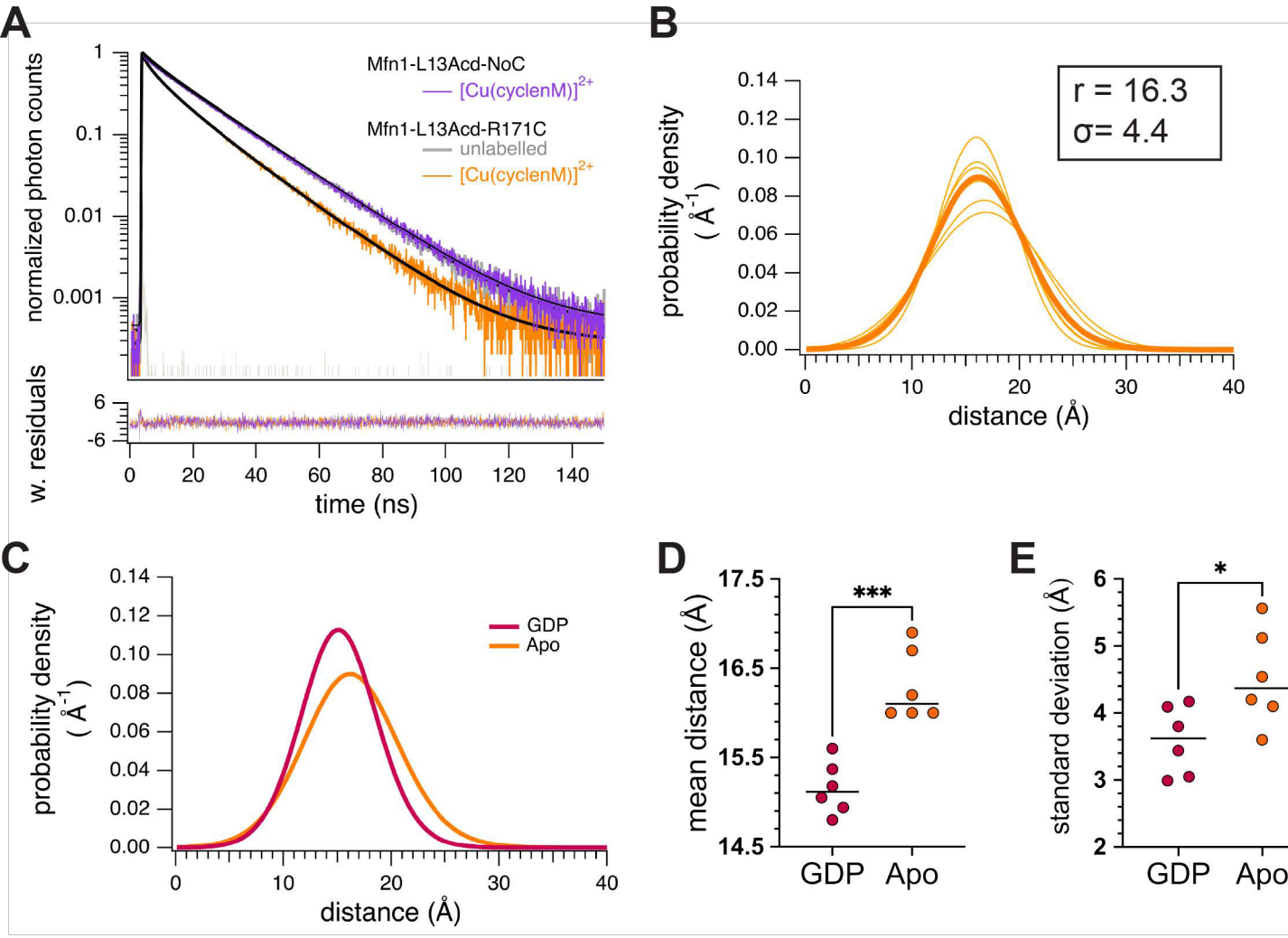

Figure 6 Steady-state lifetime tmFRET of mini-Mfn1 in the apo state. (A) Representative TCSPC data with either donor only (Mfn1-L13Acd-NoC) after (violet) the addition of [Cu(cyclenM)]2+ or from mini-Mfn1-L13Acd-R171C before (grey) and after (orange) the addition of $[Cu(cyclenM)]^{2+}$. **(B)** Spaghetti plot of distributions from individual experiments with no nucleotide bound. The average distribution is displayed in bold. **(C)** Spaghetti plot of average distributions for GDP (magenta) and apo (orange). **(D)** Mean distances for individual experiments in the presence of GDP or no nucleotide, identifying a statistical difference between the conditions. **(E)** Sigma for individual experiments when in the presence of GDP or no nucleotide, identifying a statistical difference between the conditions.

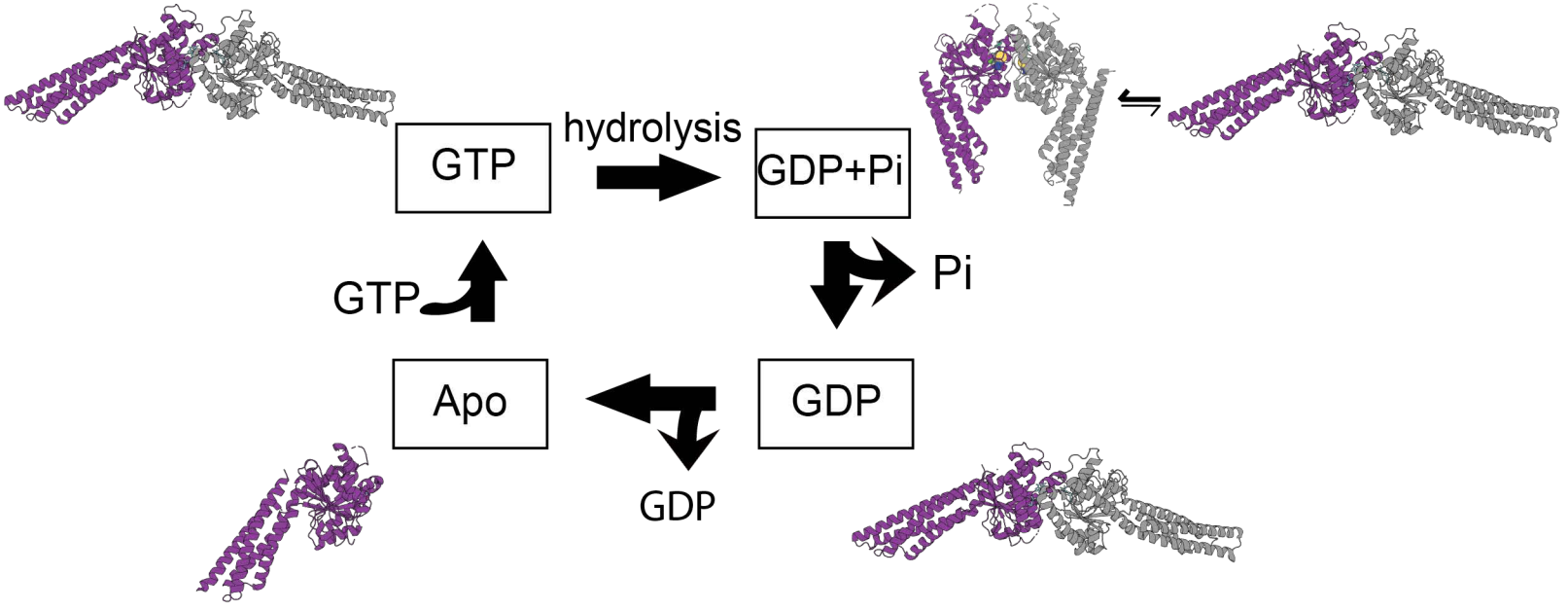

Figure 7 A model for the conformational changes driven by the catalytic cycle of Mfn1. Our data demonstrate that the GTPase and HB1 domains are in the open state for GTP-Mfn1, which supports membrane tethering. GTP hydrolysis results in GDP+Pi in the binding pocket and our data indicate an equilibrium between open and closed, with the closed state favored. Release of Pi results in GDP-Mfn1, which is in the open state. When GDP is released and Mfn1 is in the apo state, our data indicate that the GTPase domain and HB1 are in unique positions compared to the other states.